Exploring Cherenkov Emission of BGO for TOF-PET

Nicolaus Kratochwil, Etiennette Auffray, *Member, IEEE*, and Stefan Gundacker, *Member, IEEE*

***Abstract*—Bismuth germanate (BGO) was the preferred crystal for positron emission tomography (PET) scanners, but was substituted with the emergence of faster crystals. Improvements in silicon photomultipliers (SiPMs) and the use of fast high frequency readout make it possible to use the prompt Cherenkov emission in BGO in order to boost the achievable coincidence time resolution (CTR) significantly. The large fluctuations in the detected Cherenkov photon yield are causing time or amplitude walk effects in the leading edge time discrimination, which are corrected by measuring the initial signal rise time via a double threshold system. Further a classification of "fast" and "slow" timing events is shown to make best use of all the information and upgrades the CTR for most of the 511-keV events. In order to assess the practicability of this novel approach various crystal geometries and state-of-the-art SiPMs from HPK, Ketek, Broadcom, and FBK have been evaluated with the focus on the applicability in total body PET systems. For typical PET sized crystals (3 × 3 × 20 mm^3) coupled to area matching 3 × 3-mm^2 Broadcom SiPMs a time resolution of 261 ± 8 ps full width at half maximum (FWHM) was measured when applying time walk corrections, while the CTR of individual types of events with different Cherenkov yield range from 205 to 302-ps FWHM. A further thorough discussion and prospects of TOF-PET with BGO are given, especially in view of timing event classification of all detected 511-keV events, corresponding to various time of flight kernels ranging from high to low time resolution.**

***Index Terms*—Cherenkov emission in Bismuth germanate (BGO), scintillators, semiconductors, signal processing, time-of-flight (TOF) positron emission tomography (PET).**

I. Introduction

SCINTILLATORS based on lutetium (LSO, LYSO, LGSO) are commonly used crystals for positron emission tomography (PET) since 2000, being bright, fast, and achieve a good time resolution, which immediately allowed to reduce the coincidence time window (for random rejection) and to further establish time of flight (TOF). At the moment commercial PET detectors based on L(Y)SO are limited to about 200 ps coincidence time resolution (CTR) full width at half maximum (FWHM) [1] and will not lead to the desired time resolution of about 10 ps [2].

The timing capabilities of a scintillator scales with the square root of its decay time $\sqrt{\tau_d}$ and rise time (RT) $\sqrt{\tau_r}$ and the inverse square root of its light output [3], limiting the best achievable time resolution when using standard scintillation. The detection of prompt photons is one viable avenue to push for 10 ps TOF-PET imaging [4].

Bismuth germanate ($Bi_4Ge_3O_{12}$) was used in the past for PET, as it combines excellent stopping power with a high photo fraction [5]. Nowadays electronics [6], [7] in combination with silicon photomultipliers (SiPMs) having a high photon detection efficiency (PDE) and excellent single photon time resolution (SPTR) lead to the revival of BGO, as cost effective material in TOF-PET due to its pronounced Cherenkov radiation [8] with the possibility of acting as an ultraprecise time marker [9].

BGO has a density of 7.1 g/cm^3 with a peak scintillation emission at 480 nm. The refractive index is between 2.1 (600 nm) and 2.4 at the cutoff wavelength of 305 nm [10]. The intrinsic light yield for the scintillation is 10.7 ± 1.1 ph/keV with a decay time of 45.8 ns (8%) and 365 ns (92%) [11]. The Cherenkov photon yield for 511-keV photon absorption was estimated by a time correlated single photon counting measurement to be 17 ± 3 photons produced in the 310–850-nm range [11].

Recently, several groups have been contributing in the study of BGO for TOF-PET, including measurements with digital SiPMs [12], microchannel plate PMTs exploring double sided readout [13] or analog SiPMs and high frequency readout [7], [14] as well as simulations on light transport [15] and prospects for timing with improved analog and digital SiPMs [11].

While pulse shape discrimination is well established, the idea of separating events based on the signal RT of the SiPM signal was introduced in [16]. A similar approach applied to BGO allows to classify events based on their timing performance and further to correct the time walk (TW) introduced by different number of detected Cherenkov photons [17].

In this contribution, we extend the method of event classification and correction to investigate different BGO crystal cross sections and lengths, which gives an answer to the applicability of this novel method to real PET detector systems. We discuss the impact of SiPM properties on the timing performance for different commercial available SiPMs and give prospects for TOF-PET reconstruction with multiple timing kernels on the example of BGO.

Manuscript received May 28, 2020; revised August 4, 2020; accepted October 6, 2020. Date of publication October 13, 2020; date of current version September 2, 2021. *(Corresponding author: Nicolaus Kratochwil.)*

Nicolaus Kratochwil is with the Department of EP-CMX, CERN, 1211 Meyrin, Switzerland, and also with the University of Vienna, 1010 Vienna, Austria (e-mail: nicolaus.kratochwil@cern.ch).

Etiennette Auffray is with the Department of EP-CMX, CERN, 1211 Meyrin, Switzerland.

Stefan Gundacker is with the Department of EP-CMX, CERN, 1211 Meyrin, Switzerland, also with UniMIB, 20126 Milano, Italy, and also with the Department of Physics of Molecular Imaging Systems, Institute for Experimental Molecular Imaging, RWTH Aachen University, 52074 Aachen, Germany.

Color versions of one or more figures in this article are available at https://doi.org/10.1109/TRPMS.2020.3030483.

Digital Object Identifier 10.1109/TRPMS.2020.3030483

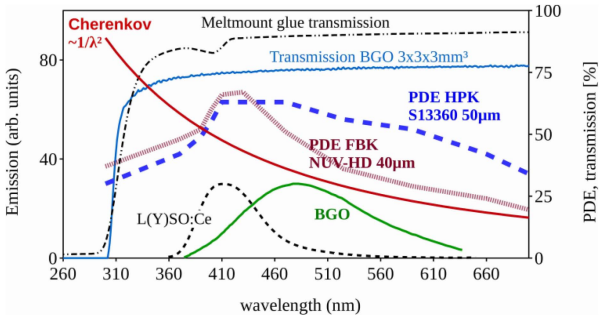

Fig. 1. Emission spectra of BGO and Cherenkov radiation compared to the PDE of SiPMs from FBK and HPK with overlapping transmission of BGO and used Meltmount glue. Modified from [11].

TABLE I
OVERVIEW OF SIPMS USED IN THIS STUDY

SiPM producer	SPAD size [μm^2]	SiPM size [mm^2]	bias voltage [V]	$SPTR_{intr}$ FWHM [ps]	Single SPAD[2] amplitude [mV]
HPK S13360	50x50	3x3	62	135[1]± 8	87 ± 5
HPK S14160	50x50	3x3	48	117[1]± 6	90 ± 5
Ketek PM3350	50x50	3x3	37	74[1]± 6	50 ± 4
Broadcom S4N33	30x30	3x3	38	78 ± 6	44 ± 3
FBK NUV-HD	40x40	4x4	39	69[1]± 6	44 ± 3

[1] Values taken from [11].
[2] Measured at stated SiPM bias voltage.

II. MATERIALS

A. BGO Crystals

The crystals used in this study were bought from Epic-Crystals and are fully polished. The tested crystals have a cross section of 1 × 1, 2 × 2, and 3 × 3 mm^2 with a length ranging from 3 mm up to commonly used sizes in PET of 15, 20, and 30 mm. The crystals were wrapped with more than 5 layers of Teflon and optically coupled to the SiPMs with Cargille Meltmount ($n = 1.582$).

B. Silicon Photomultiplier

The list of SiPMs used in this study is given in Table I. For all SiPMs a bias voltage scan was performed to find the best operation point as stated in the table. The intrinsic SPTR values are taken from [11] (HPK, Ketek, FBK) or measured with the setup and methods described in [11] (Broadcom). The SiPMs from Hamamatsu have higher PDE close to the emission of BGO, while FBK, Broadcom, and Ketek are more optimized close to the emission spectrum of L(Y)SO, shown in Fig. 1. Both types of SiPMs from Hamamatsu and Ketek have the same cross section of 3 × 3 mm^2 and single photon avalanche diode (SPAD) size of 50 × 50 μm^2. The used SiPMs from FBK (NUV-HD) have a larger cross section (4 × 4 mm^2) and 40-μm SPAD pitch without protective resin and benefit from direct coupling of the crystal to the SiPM via high refractive index glue without having the lower refractive index protective window in between giving better light transfer efficiency (LTE). The larger active area of this SiPMs allows to study the impact of the crystal cross section on the CTR, without any impact of light loss from the crystal edges. The FBK NUV-HD has been commercialized by Broadcom and the AFBR-S4N33C013 device was included in the measurements (3 × 3 mm^2 active area). The SiPMs from Hamamatsu are commercially available [18].

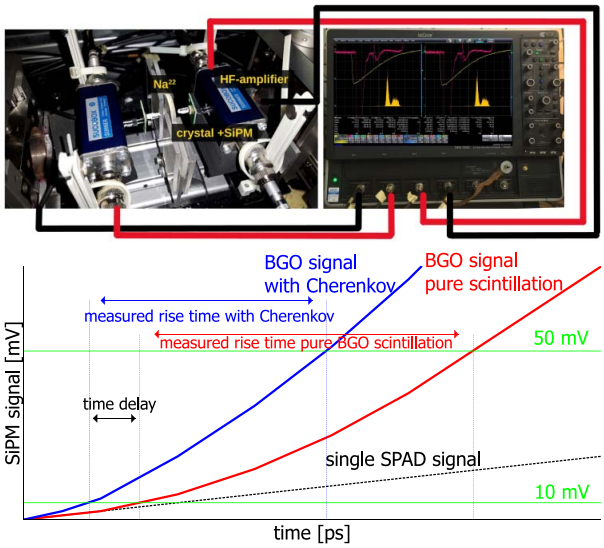

Fig. 2. (Top left): CTR setup with source, crystals, and HF-amplifier. (Top right): Picture of the oscilloscope with the energy and time signals. (Bottom): Illustration of RT separation. Events having Cherenkov photons (blue) detected on top of scintillation photons pass the leading edge threshold faster and have a smaller value of the RT compared to only BGO scintillating photons (red) detected.

C. Coincidence Time Resolution Setup

The CTR was measured with the setup described in [7]. A ^{22}Na source emits two gammas back to back which are detected in coincidence by the BGO crystals coupled to SiPMs. The signal is split, one part is read out by the high frequency electronics for the time signal, the other part is amplified using an analog operational amplifier for the energy signal. The energy signal integration gate was set to 160 ns. The obtained charge histogram was fitted to a Gaussian function assuming the center to be 511 keV. Events were accepted in an energy range of 440 and 665 keV, in agreement with clinical TOF-PET scanners [19]. Using a narrower energy window selection (e.g., 500 to 665 keV) would slightly improve the time resolution, but at the same time decrease the number of coincidence events by a factor of 3 and therefore spoil the good sensitivity of BGO [17]. A picture of the setup and readout channels is shown on the top of Fig. 2.

The leading edge threshold is set on the oscilloscope (LeCroy DDA735Zi) to calculate the coincidence time difference of the signal crossing via linear interpolation to be scanned in a range between 2 and 100 mV. In addition the signal RT, which is the time difference between the signal crossing at 10 and 50 mV, is recorded and analyzed for both channels. This RT measurement is illustrated at the bottom of Fig. 2. The offline analysis is done with ROOT [20].

III. DATA ANALYSIS

In this section, the data analysis and CTR correction methods are described.

A. Modeling the Time-Delay Distribution

The high frequency readout allows to make best use of the few Cherenkov photons detected due to the fast SiPM signal RT, low electronic noise and low leading edge threshold

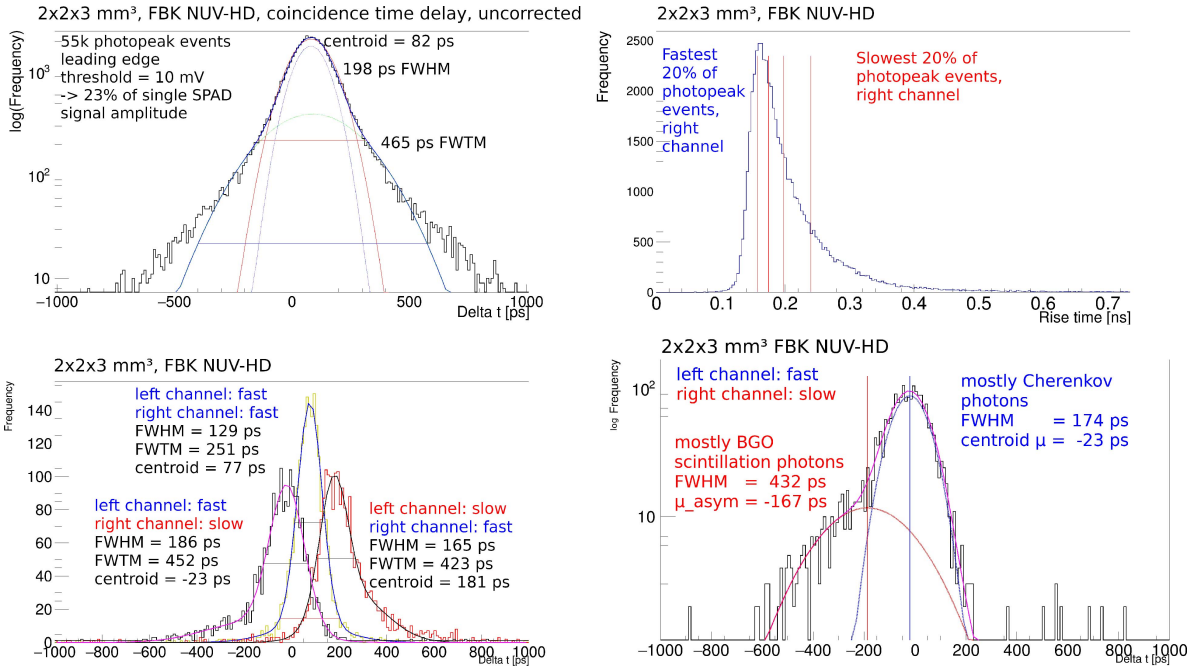

Fig. 3. (Top left): Coincidence time delay fitted with a double-Gaussian function (blue) and individual Gaussian contributions (dotted). In contrast a single Gaussian fit function (red) is not fitting the measured data. (Top right): Histogram of measured RT divided into five different categories with equal numbers. (Bottom left): Coincidence time delay for three different RT categories before correction. (Bottom right): Semi logarithmic coincidence time delay for one category (fast-slow) illustrating the asymmetry and the tail on the left side caused by different number of detected Cherenkov photons.

applicable. However, the number of Cherenkov photons detected show large fluctuations from event to event ranging from a high detected Cherenkov photon number to no prompt photons detected at all, where the timestamps are determined solely by the BGO scintillation. An example of the coincidence time-delay distribution is shown on the top left of Fig. 3. To model this distribution, a double-Gaussian fit described in ((1)) is used, where the first part models the time delay coming mainly from Cherenkov photons having an abundance of r_C and standard deviation of σ_C and the second part describes the events where only scintillation photons from the BGO emission is detected with abundance $1 - r_C$ and standard deviation σ_S

$$y_{\text{fit}} = \frac{A \cdot r_C}{\sigma_C} \cdot \exp\left(-\frac{(x-\mu)^2}{2\sigma_C^2}\right) + \frac{A \cdot (1-r_C)}{\sigma_S} \cdot \exp\left(-\frac{(x-\mu-\mu_{\text{asym}})^2}{2\sigma_S^2}\right). \quad (1)$$

The factor A is a normalization factor which depends on the acquired statistics and bin size and μ is the center of the distribution. The term μ_{asym} is zero, if the number of detected Cherenkov photons is the same for both sides, which is the default case when all photopeak events without further selection are used. In the case of multi kernel classification, which is more in detail discussed in Section VI-B, this term is nonzero and responsible for an asymmetry in the CTR distribution. This asymmetry is visualized in the bottom right of Fig. 3 in a semi logarithmic plot of the time delay of one category.

B. Time Resolution Classification and Correction

Depending on the number of Cherenkov photons detected, the timing signal is passing earlier or later the leading edge threshold which is causing a TW in the range of hundreds of picoseconds [17], illustrated at the bottom of Fig. 2. Furthermore, signals with a higher number of Cherenkov photons detected have a smaller RT value. To correct for this TW two different methods are used, namely, *classification method* and *fit method*.

1) Classification Method: The first type of correction was introduced in [17]. Histograms of the RTs (RT_l, RT_r) of both channels are drawn as shown on the top right of Fig. 3 and the coincidence events are divided into 5×5 categories with equal number of counts. The combination gives in total 25 categories of events, each containing 4% of the photopeak events. Three delay time histograms are shown at the bottom left of Fig. 3, illustrating different categories. The time resolution as well as the centroid of the distribution change with different categories. The correction aligns the time delay of all categories based on the centroid (μ) before merging them together.

The time-delay distribution for categories, where the channels have a different number of Cherenkov photons detected is no longer symmetric meaning that μ_{asym} is nonzero. This asymmetry is illustrated on the bottom right of Fig. 3, where for the left channel mainly Cherenkov photons are detected while for the right side mainly scintillation photons.

The advantage of this method is, that individual time resolution categories are constructed, such that each category can be allocated to its corresponding timing kernel and used individually. The disadvantage is, that a high number of events is needed to determine the correction coefficients. If not stated otherwise, this is the default method used for the correction.

2) Fit Method: The other way to correct, here labeled *fit method*, directly corrects for the RT induced TW for each coincidence event i according to

$$\hat{t}_i = t_i - \text{TW}(\text{RT}_l, \text{RT}_r). \quad (2)$$

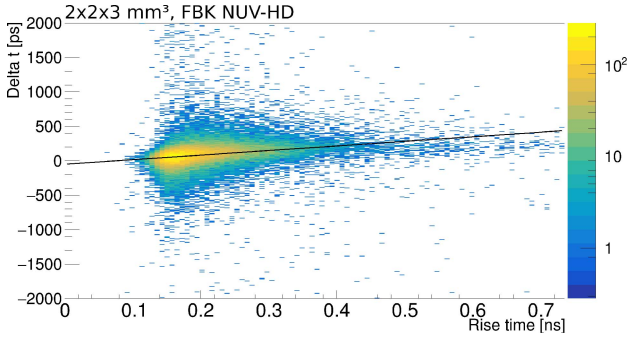

Fig. 4. Scattered plot of the measured time delay against the RT of the right channel, including the linear fit function used.

A scattered plot of the time delay against the signal RT per channel is drawn, shown in Fig. 4. A linear fit function ($p_0 + p_1 \cdot$ RT) is used to determine the correction coefficient for the left (l) and right (r) side. The TW and therefore the measured time delay depend on the signal RT of both channels TW(RT$_l$, RT$_r$), but each side contributes individually such that (3) can be used to correct for the contribution of both sides simultaneously according to (4), where the correction coefficients are subtracted for the left and right side for each time delay t_i

$$\mathrm{TW}(\mathrm{RT}_l, \mathrm{RT}_r) = 0.5 \cdot \mathrm{TW}_l(\mathrm{RT}_l) + 0.5 \cdot \mathrm{TW}_r(\mathrm{RT}_r) \quad (3)$$

$$\hat{t}_i = t_i - 0.5 \cdot \left(p_{0,l} + p_{1,l} \cdot \mathrm{RT}_l + p_{0,r} + p_{1,r} \cdot \mathrm{RT}_r\right). \quad (4)$$

The advantage of this method is, that it is easy to implement and works also with low statistics ($\approx$ 500 coincidence photopeak events) but is not as accurate and does not construct multiple event categories. In the contribution, this method is solely used for the correction of leading edge threshold scans since lower statistics were used.

IV. Time Resolution Measurement Results

In Section IV-A, the timing performance for small $2 \times 2 \times 3$ mm^3 BGO crystals is presented for different SiPMs. Section IV-B shows time resolution results for crystals matching the size of the SiPM surface (3×3 mm^2) for 3 and 20-mm long crystals. In Section IV-C, the impact on timing performance of crystal aspect ratio is evaluated.

A. CTR Achieved With Different SiPM Types

To evaluate the influence of SiPM properties on the CTR a leading edge threshold scan ranging from 2 up to 100 mV was performed for the SiPMs coupling $2 \times 2 \times 3$ mm^3 BGO crystals. As the SiPMs have different single SPAD signal amplitude the threshold was normalized to the individual amplitudes. The uncorrected results are shown on the top of Fig. 5. It can be observed that the best results are achieved by setting the threshold to just above the noise floor of the SiPM (around 6–8 mV), which is in agreement with the findings in [7] and [14]. Two types of SiPMs show very similar timing performance of 185 $\pm$ 6 ps FWHM (FBK NUV-HD) and 189 $\pm$ 6 ps FWHM (HPK S14160).

At the bottom of Fig. 5 the time resolution results after TW correction, according to (4), are shown. Although the

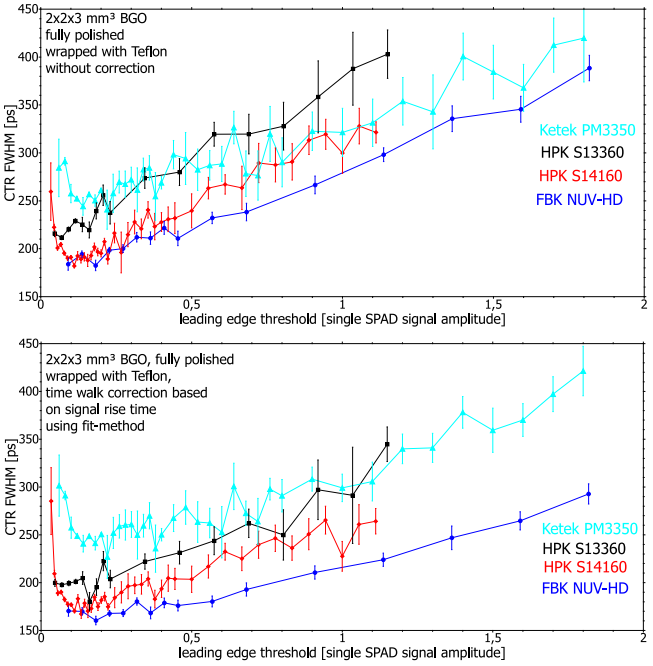

Fig. 5. Leading edge threshold scan of all SiPMs before (top) and after (bottom) TW correction with the fit method. The x-axis is normalized to the measured single SPAD signal amplitude of the SiPMs.

timing performance improves for all tested SiPMs, FBK benefits to a larger extent from this correction with an achieved CTR value of 160 $\pm$ 4 ps FWHM. After correction the best threshold value is no longer at very low threshold values, but stays almost constant up to $\approx$ 50% of the single SPAD signal amplitude, meaning that finding the best settings becomes less critical. Measurements with increased statistics were performed for all devices at 10 mV and the results are summarized in Table II.

B. Time Resolution Results for Crystals Matching the SiPM Size

For a TOF-PET scanner it is important to have a high sensitivity while keeping the number of readout channels low. Therefore, emphasis must be put to match the SiPM active area with the crystal cross section, e.g., having 3×3 mm^2 BGO cross section coupled to a 3×3 mm^2 SiPM. On top of Fig. 6 threshold scans are shown for $3 \times 3 \times 3$ mm^3 sized crystals. A time resolution degradation of 8% (160 $\pm$ 3 ps $\rightarrow$ 173 $\pm$ 3 ps) for FBK and up to 26% (236 $\pm$ 7 ps $\rightarrow$ 298 $\pm$ 7 ps) for Ketek compared to the results for smaller cross section is observed. One part of this deterioration comes from light loss at the edges of the crystal, as some light can escape and is not detected [21]. In addition there can be some light loss for crystals being not perfectly aligned, a combination of vertical and horizontal displacement of 0.2 mm would lead already to a light loss of $\approx$15%. The impact on the crystal cross section is discussed more in detail in Section IV-C.

The threshold scan for $3 \times 3 \times 20$ mm^2 crystal geometry is shown on the bottom of Fig. 6. For 20-mm crystal length an increase of the time resolution by $\approx$100 ps compared to 3-mm length with the same cross section is observed. The trend of

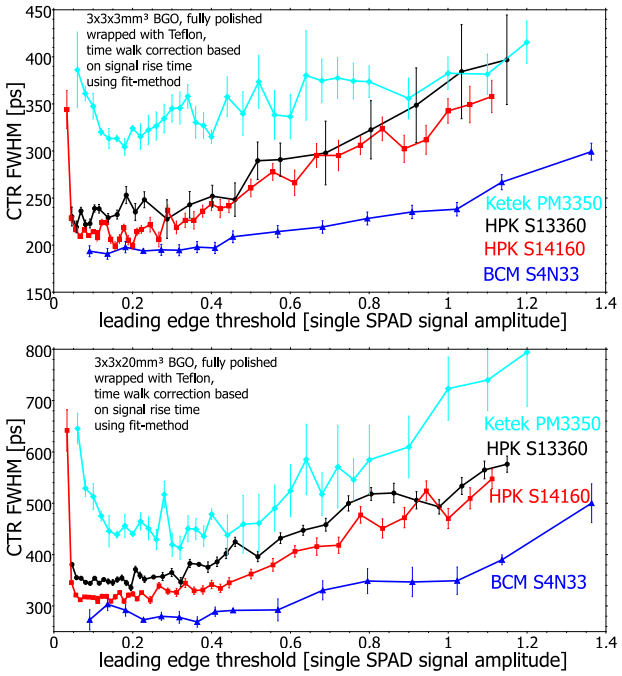

Fig. 6. Leading edge threshold scan after TW correction (fit method) for $3 \times 3 \times 3$ mm^3 (top) and $3 \times 3 \times 20$ mm^3 (bottom).

TABLE II
SUMMARY OF TIMING PERFORMANCE FOR VARIOUS CRYSTAL GEOMETRIES, INCLUDING CONTRIBUTION AND ABUNDANCE OF INDIVIDUAL CTR CONTRIBUTIONS

SiPM producer	Geometry [mm^3]	first Gaussian[1] FWHM [ps]	second Gaussian[2] FWHM [ps]	r_C[3] [%]	CTR[5] FWHM [ps]
HPK S13360	1x1x3	152 ± 5	362 ± 11	56 ± 3	178 ± 5
HPK S13360	1x1x15	232 ± 10	673 ± 29	55 ± 4	267 ± 11
HPK S13360	2x2x3	162 ± 4	417 ± 11	54 ± 3	188 ± 5
HPK S13360	2x2x5	186 ± 7	490 ± 17	59 ± 3	213 ± 8
HPK S13360	2x2x10	188 ± 7	523 ± 18	44 ± 3	237 ± 8
HPK S13360	2x2x15	229 ± 10	736 ± 28	48 ± 3	278 ± 10
HPK S13360	2x2x20	229 ± 12	727 ± 33	42 ± 3	290 ± 11
HPK S13360	2x2x30	281 ± 14	916 ± 38	47 ± 3	342 ± 13
HPK S13360	3x3x3[4]	211 ± 7	754 ± 23	56 ± 3	237 ± 7
HPK S13360	3x3x15[4]	256 ± 9	930 ± 29	42 ± 2	320 ± 9
HPK S13360	3x3x20[4]	268 ± 8	1020 ± 27	39 ± 2	345 ± 8
HPK S13360	3x3x30[4]	309 ± 13	1180 ± 42	41 ± 3	385 ± 16
Ketek PM3350	2x2x3	200 ± 8	640 ± 32	58 ± 3	236 ± 7
Ketek PM3350	3x3x3[4]	246 ± 8	880 ± 35	48 ± 3	298 ± 7
Ketek PM3350	3x3x20[4]	300 ± 11	1209 ± 38	33 ± 2	425 ± 13
HPK S14160	2x2x3	141 ± 4	357 ± 10	49 ± 4	174 ± 6
HPK S14160	3x3x3[4]	174 ± 4	551 ± 22	51 ± 3	206 ± 8
HPK S14160	3x3x20[4]	244 ± 8	923 ± 29	40 ± 2	308 ± 11
BCM S4N33	2x2x3	130 ± 6	381 ± 18	59 ± 4	150 ± 11
BCM S4N33	3x3x3[4]	164 ± 5	665 ± 19	60 ± 2	181 ± 4
BCM S4N33	3x3x20[4]	220 ± 5	987 ± 31	45 ± 2	261 ± 8
FBK NUV-HD	1x1x3	125 ± 4	308 ± 10	68 ± 2	137 ± 3
FBK NUV-HD	1x1x15	188 ± 5	619 ± 20	56 ± 2	217 ± 4
FBK NUV-HD	2x2x3	147 ± 4	458 ± 13	67 ± 3	160 ± 3
FBK NUV-HD	2x2x15	185 ± 5	723 ± 20	51 ± 2	215 ± 4
FBK NUV-HD	3x3x3	159 ± 5	467 ± 15	68 ± 2	173 ± 3
FBK NUV-HD	3x3x15	200 ± 5	742 ± 23	51 ± 2	234 ± 4

[1] Mostly Cherenkov photons.
[2] Mostly scintillation photons.
[3] Abundance of Gaussian fit coming mostly from Cherenkov photons.
[4] Crystal cross section is matching the SiPM active area.
[5] After correction using classification method.

getting better time resolution values for BCM S4N33 is the same for both tested geometries.

Results for measurements with higher statistics and correction based on the classification-method are summarized in Table II together with additional results for various crystal geometries.

C. Impact of Crystal Aspect Ratio on the Timing Performance

To further investigate the impact of crystal length and cross section on the timing performance measurements with 1×1, 2×2, and 3×3 mm^2 BGO cross section and 3 mm or 15-mm crystal lengths were performed with FBK NUV-HD (4×4 mm^2 active area). As finding the best leading edge threshold is less critical, measurements with higher statistics were performed at 10-mV threshold (22% of single SPAD signal amplitude), always at the same temperature and bias voltage. The measured coincidence time-delay histograms are shown in Fig. 7, where the y-axis is in logarithmic scale to better identify the tails. It is to mention, that less than 1% of the coincidence events are outside of the double-Gaussian distribution and are coming mainly from SiPM dark count events. As the trigger is put below one photoelectron it can happen, that a dark count event fires on one channel before the real signal is detected. When using a second validation trigger at higher threshold values the tails outside of the double-Gaussian distribution decrease.

The use of higher statistics in combination with the classification method allows to construct categories with different CTRs, where the fastest and slowest category is given on the top right of each figure. The analysis of different categories is discussed more in detail in Section VI-B. When increasing the crystal cross sections from 1×1 mm^2 to 3×3 mm^2 the time resolution in terms of FWHM and FWTM is getting worse. For 15-mm long crystals no improvement for the smallest cross section of 1×1 mm^2 compared to 2×2 mm^2 can be noticed with FBK, within the measurement errors. Additionally to the lower LTE in high aspect ratio crystals, a lower impact of the external optical cross-talk most likely plays a role in this case [22]. Because external cross-talk has to traverse the whole 15-mm crystal length twice when reflected back to the SiPM, hence, these crosstalk photons simply come too late to impact the CTR significantly. This is not the case for 3-mm long crystals, as can be seen in Fig. 7. For 3×3 mm^2 cross section, the overall timing performance as well as the contribution coming from the individual Gaussian functions is deteriorating compared to smaller cross sections.

In addition to the measurements with FBK, more crystal lengths and cross sections were measured with HPK S13360. These measurements are summarized in Fig. 8 and Table II. For 3×3 mm^2 crystal cross section an additional CTR deterioration is observed due to light loss on the edges, as it matches the active area of the SiPM. Comparing 15 and 30 mm results the CTR marginally deteriorates from 278 ± 10 to 342 ± 13 ps FWHM for 2×2 mm^2 cross section and from 320 ± 9 to 385 ± 16 ps for 3×3 mm^2 cross section.

V. DISCUSSION

A. Impact of SiPM Properties on Timing Performance

When looking at the performance of the SiPMs for small crystal sizes shown in Fig. 5 both HPK S14160 and FBK NUV-HD have very similar timing performances. The reason for this is due to the interplay of SPTR and PDE for the Cherenkov emission. SiPMs from Hamamatsu have slightly

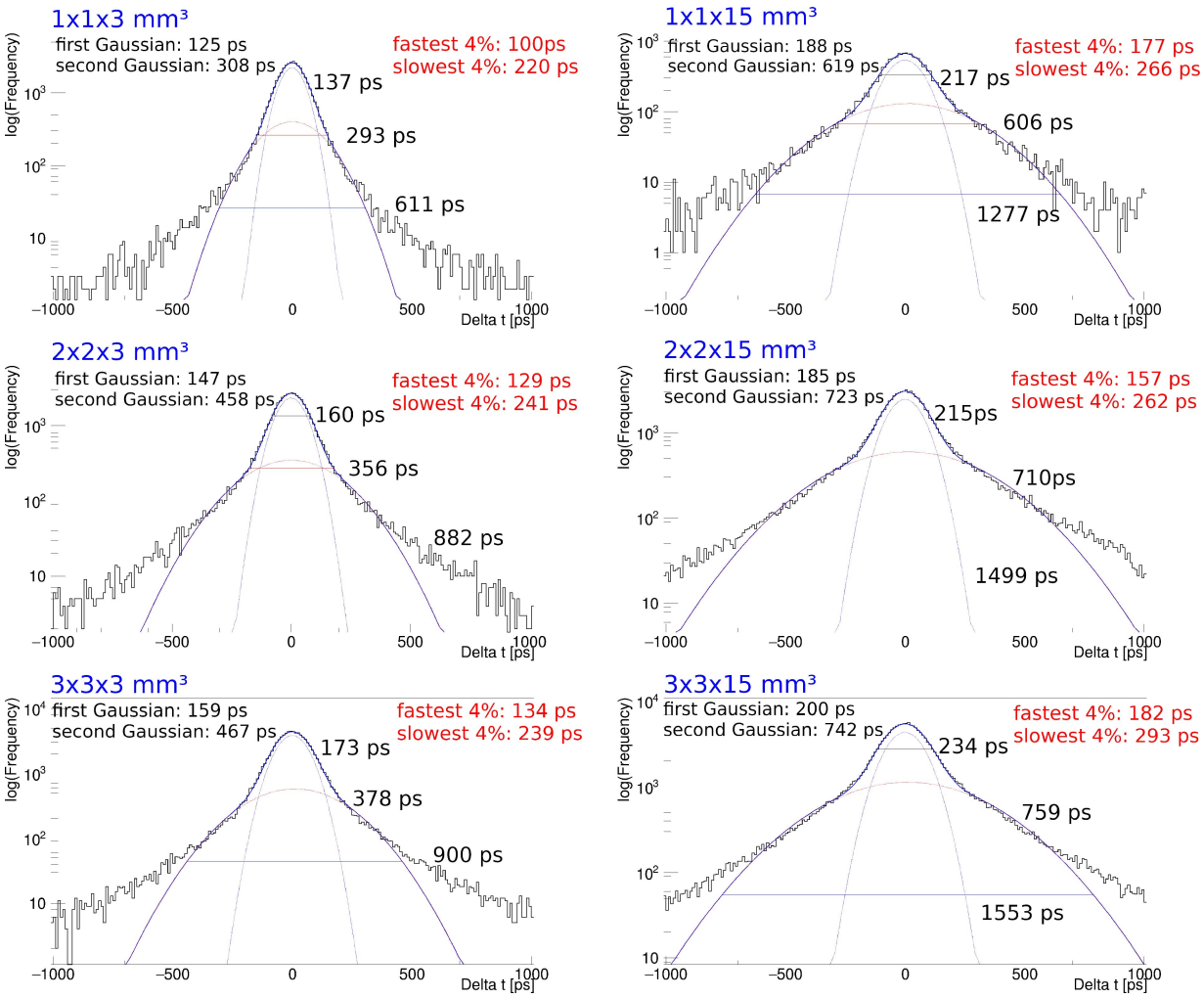

Fig. 7. Time-delay histogram after TW correction for different cross section and lengths coupled to FBK NUV-HD at 10 mV (22% of single SPAD signal amplitude) leading edge threshold. The dotted lines in blue and red are the individual contributions of the double-Gaussian fit function. CTR values in red (FWHM) represent the best (highest number of detected Cherenkov photons) and worst (lowest number of detected Cherenkov photons) category. The values next to the lines represent the CTR in terms of FWHM, FWTM, and FW100M of the time-delay distribution.

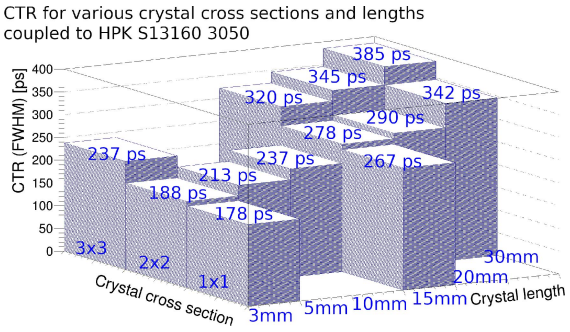

Fig. 8. Illustration of time resolution after TW correction for different crystal lengths and cross sections measured with HPK S13360.

higher PDE weighted over the Cherenkov emission, as they benefit from extended PDE at longer wavelengths and detect the few Cherenkov photons emitted at larger wavelength. On the other hand the used SiPMs from FBK benefit from outstanding intrinsic SPTR of 69 ± 6 ps FWHM, compared to the decent SPTR of 117 ± 6 ps for HPK S14160. In particular for scintillators with negligible RT and/or pronounced Cherenkov emission the SPTR crystallizes as a crucial parameter [3], [11]. Comparing SPTR values in Table I with the CTR results in Table II the trend of better SPTR causing better time resolution is the same for both types of Hamamatsu and FBK.

Based on the SPTR solely, also a good CTR was expected for SiPMs from Ketek. The threshold scans indicate, however, that this SiPMs have larger DCR and cross-talk as the optimal threshold value is shifted to larger thresholds which is in contradiction to the trend of all other SiPMs. In [24], it is reported that optical crosstalk events can significantly deteriorate the best timing achieved with SiPMs, especially in the case of light sources with low intensities, as in the case of BGO and Cherenkov emission. This could be the reason why Ketek SiPMs perform quite well when coupling to bright LSO reported in [11], although worse when detecting the faint Cherenkov signal from BGO. Measurements of DCR and cross-talk probability are foreseen for all tested devices to confirm this assumption.

The SiPMs from Broadcom perform very similar as the FBK NUV-HD SiPMs as they have similar technology. However, for $3 \times 3 \times 3$ mm^3 BGO the performance is slightly

worse than FBK (181 ± 4 ps FWHM for FBK compared to 173 ± 3 ps FWHM for Broadcom). Possible explanations are light loss at the crystal edges, better LTE for the FBK devices as they have no protective resin and/or a slightly better intrinsic SPTR for FBK SiPMs.

Comparing the time resolution results in this study with a digital approach (Philips digital photon counter, DPC) we see an improvement from 200 ps FWHM [12] to 173 ps for $3 \times 3 \times 3$ mm^3 BGO crystals measured with FBK and from 330 ps (DPC) to 261 ps (Broadcom) FWHM for $3 \times 3 \times 20$ mm^3 while matching the active area of the SiPM with the crystal cross section. The SPTR of the digital SiPM was measured to be 103-ps FWHM [25], but has lower PDE compared to the tested analog SiPMs. Simulations [11] point toward an advantage of the digital first photon approach over analog SiPMs for good SPTR and PDE values.

The results presented in this study are even better compared to a double sided readout approach obtaining 331 ps for $3 \times 3 \times 20$ mm^3 [13] with FBK NUV-HD SiPMs. In this case the few produced Cherenkov photons are split on both sides, meaning the electronic noise contributes for both readout channel lowering the signal to noise ratio (SNR). In [26] it was shown, that dividing the produced photons into different SiPMs lead to a deterioration due to increased excess noise.

Using HF-readout and FBK NUV-HD SiPMs the same time resolution for $3 \times 3 \times 3$ mm^3 (200 ± 3 ps FWHM) and $3 \times 3 \times 15$ mm^3 (277 ± 7 ps FWHM) [14] as in this contribution were measured, when not correcting for the TW (202 ± 3 ps FWHM and 278 ± 5 ps). This is expected, as from the physics point of view the same measurement was performed. Small differences can occur as the photopeak was narrower and a Lorentz fit function instead of a double Gaussian function was used in [14].

After correction for the RT induced TW a time resolution of 151 ± 3 ps is reported [17] for $2 \times 2 \times 3$ mm^3 crystal geometry, again using HF-readout and FBK NUV-HD SiPMs. For this study the crystals were depolished opposite to the readout side which is increasing the light output for this geometry and therefore improving the achieved CTR compared to 160 ps summarized in Table II.

B. Impact of Crystal Geometry on Timing Performance

We observe a deterioration of time resolution when increasing the crystal cross section. Besides possible alignment and light loss on the edges there are more parameters involved. First, for smaller crystal surface a narrower region of SPADs is activated, which effectively decreases the SPTR [22], [23]. Another effect is the increase of external cross-talk probability when covering a larger SiPM area by the crystal, which acts as a reflector. For the case of Ketek the large deterioration of 27% in time resolution when changing the crystal geometry from $2 \times 2 \times 3$ mm^2 to $3 \times 3 \times 3$ mm^3 indicates a large impact due to crosstalk.

It is interesting to see, that a better time resolution for $1 \times 1 \times 3$ mm^3 crystal geometries is measured compared to $2 \times 2 \times 3$ mm^3. When measuring LYSO:Ce crystals with NINO readout this difference was not seen, which might be due to the slower NINO readout electronics or the fact, that LYSO:Ce produces a much stronger light signal [22]. Whether the explanation lies in the readout (NINO versus HF), the SPTR, Cherenkov photons or all of them is subject for further studies.

When further increasing the crystal length to 30 mm the time resolution does only deteriorate by $\approx 18\%$ compared to 20 mm. In this sense, if the detector design allows it, the sensitivity gain will very likely be of advantage for longer crystals than the disadvantage of a relatively small timing performance loss.

C. Correction Method

In this contribution two correction methods were used. They are from a mathematical point of view very similar, as for both cases the detected Cherenkov induced TW is corrected. While uncorrected a time resolution of 198 ± 6 ps FWHM (465 ± 14 ps FWTM) is measured for $2 \times 2 \times 3$ mm^3 BGO crystals coupled to FBK NUV-HD at 10 mV leading edge, the fit method yields a time resolution of 168 ± 6 ps FWHM (391 ± 14 ps FWTM) compared to 160 ± 4 ps FWHM (357 ± 12 ps FWTM) when using the classification method. The advantage of the classification method is, that the centroid of the time delays is better identified by a more complex fit function such that the correction coefficients can be better calculated. Also the used linear fit function might not model the TW best and a more advanced fit function should further improve the correction. However, already with this very simple function most of the TW is corrected.

Looking at the shape of the threshold scan in Fig. 5 the impact of the threshold becomes less important after correction. The leading edge threshold uses the information of all photons which have been detected before the signal has passed the threshold, which can be seen as an averaging of the preceding photoelectron timestamps [27]. Photons which arrive around or after the signal crossing time of the threshold carry also information which is used to improve the time estimation by using the signal RT. In this sense, instead of using only the crossing time estimator a second time estimation is accessible allowing to treat analog SiPMs toward a digital-like approach. This weak threshold dependency at low threshold values is interesting for a system integration, as finding the optimum threshold becomes less crucial. Preliminary results further show, that the exact values of the RT thresholds is less critical, as a window between 50 and 120 mV gives very similar results as for the used 10–50-mV range. Systematic studies to fully understand the impact of the correction method on the time estimation and applied leading edge threshold together with variation of the RT ranges are foreseen.

D. Translation Linearity

To confirm the translation linearity of the correction method, measurements with four different detector positions were performed while keeping the other detector and the source at the same place. For the first measurement 70k coincidence photopeak events were measured and the cuts on the RT as well as the correction coefficients determined. For the other three measurement positions the prior determined cuts on the RT and correction values were used. The corrected time-delay histograms are shown in Fig. 9. A detector movement of 1 cm should theoretically translate in a time difference of 33.3 ps,

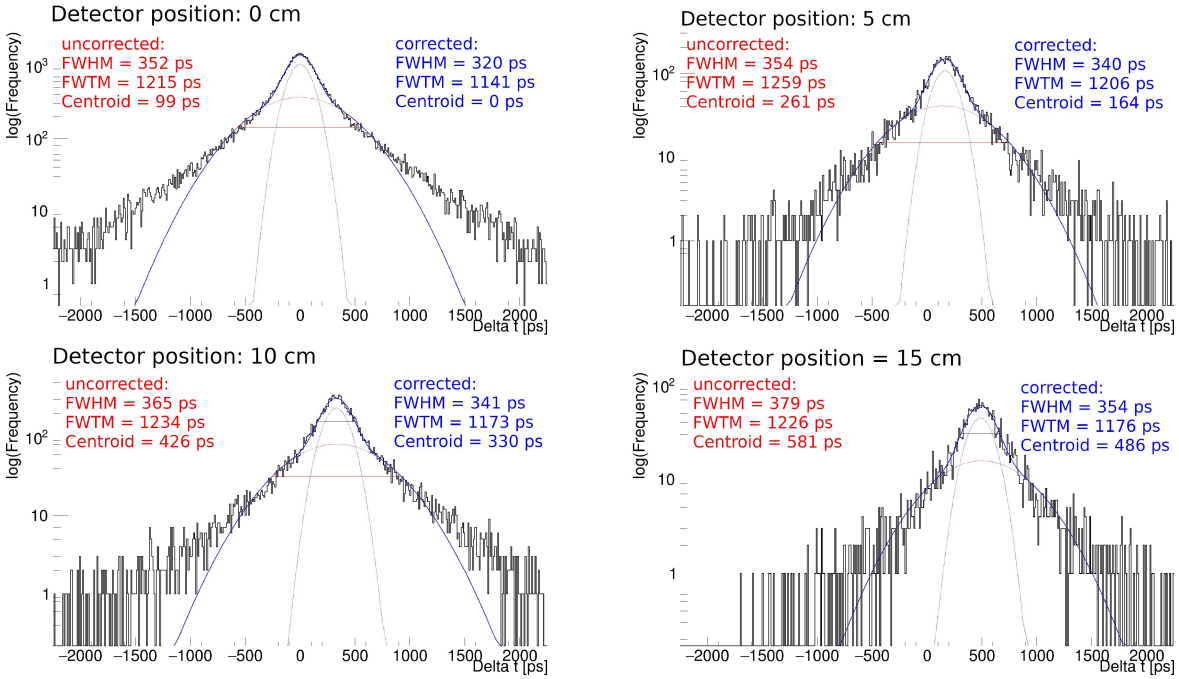

Fig. 9. Time-delay histogram for four different detector positions after correcting the TW using the first measurement as calibration. The dotted lines represent the individual contributions of the fit function.

while fitting the four corrected centroids is giving a slope of 32.5 ± 0.9 ps/cm. This measurement confirms, that the acquisition system has no flaws and the correction can be used in TOF-PET. The small deterioration in time resolution from 320 ± 8 ps FWHM (1141 ± 31 ps FWTM) for the smallest detector distance and 354 ± 18 ps FWHM (1178 ± 62 ps FWTM) for the largest detector distance could either be caused by alignment issues as some depth of interaction positions were more likely hit than others or by a change in the detected solid angle of the gammas, as for increased distance the solid angle is smaller and less likely to hit the crystals at short depth of interaction information (DOI) values.

VI. Prospects for TOF-PET With BGO

A. Estimation of Equivalent SNR

As pointed out in [28], the effective sensitivity S_{eff} and therefore the reconstructed image quality or equivalent dose reduction of a TOF-PET detector depends on the achieved time resolution but also on the single detection efficiency of the gammas η_{det} and the angular coverage η_{geom} as expressed in

$$S_{\text{eff}} \approx \frac{\eta_{\text{det}}^2 \cdot \eta_{\text{geom}}}{\text{CTR}}. \tag{5}$$

The main benefit of BGO compared to other known scintillators is its low attenuation length for 511-keV gammas together with the high photoabsorption probability, leading to the highest value of η_{det} of all known scintillators. In addition, the lower cost allows to build more detector rings to boost η_{geom} leading to a more cost effective total body PET. In order to compare the achieved time resolution values for BGO with LSO in terms of SNR, the equivalent SNR for BGO was calculated and compared with LSO having the same crystal geometry and keeping η_{geom} constant. Using the attenuation length λ_{att} (BGO: 10.4 mm, LSO: 11.4 mm) and photoelectric probability P_E (BGO: 40%, LSO: 32%) [29] the single detection efficiency as a function of the crystal length l is calculated according to

$$\eta_{\text{det}}(l) = P_E \cdot (1 - \exp(-l/\lambda_{\text{att}})). \tag{6}$$

For 15-mm BGO the single detection efficiency is $\eta_{\text{det,BGO}} = 0.31$, while for LSO it is $\eta_{\text{det,LSO}} = 0.23$. As the ratio of these two values is squared in (5), a time resolution obtained with 2 × 2 × 15 mm^3 BGO coupled to FBK NUV-HD of 215 ps gives the same SNR as a CTR of 127 ps for LSO having the same geometry. The latest PET systems based on L(Y)SO enable time resolution values as low as 200–250 ps time resolution [30]. When correcting for the detection efficiency, this translates into BGO timing of 340–425 ps which can be easily reached for long BGO crystals matching the SiPM cross section as shown in Section IV-B and Table II. One challenge, however, remains in the non-Gaussian shape of the time-delay distribution and in particular the tails. For example, the FWTM for 2 × 2 × 15-mm^3 BGO is 710 ps, giving a ratio of FWTM/FWHM of 3.3 compared to the ratio of a single Gaussian function of 1.8.

Another way to compare BGO performance to L(Y)SO-based scintillators is to look how many detected coincidences are within a coincidence time window. On the top of Fig. 10 the percentage of events within a coincidence time window are plotted for four different BGO measurements. In contrast to the measured BGO distribution are single Gaussian distribution drawn having a FWHM of 98, 213, and 430-ps FWHM representing the current lab record for 20-mm long LSO crystals [7], the timing performance of the Siemens Biograph Vision PET scanner [1] and the time resolution of the total body PET scanner Explorer [31], respectively. For the BGO

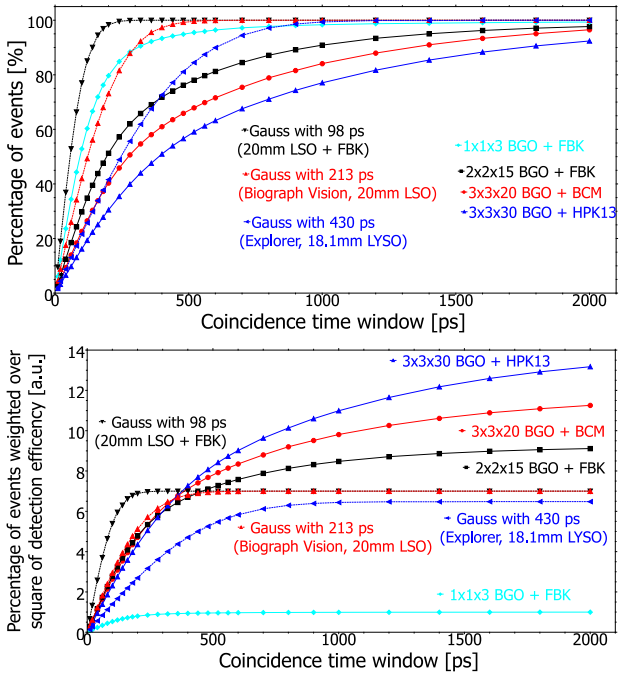

Fig. 10. (Top): Percentage of total events as function of coincidence window for four different BGO measurements in comparison to a single Gaussian fit function with different FWHM. (Bottom): Percentage of events weighted with the detection efficiency square.

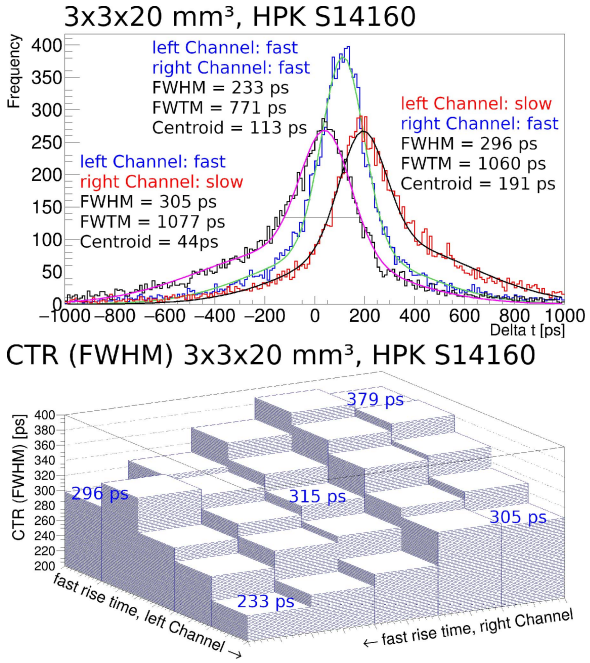

Fig. 11. (Top): Time-delay histogram with double Gaussian fit for three categories (left: fast-slow, center: fast-fast, right: slow-fast). (Bottom): CTR for all 25 timing categories for 3 × 3 × 20 mm^3 coupled to HPK S14160.

data the impact of the tails is well visible as it requires a larger coincidence time window until the majority of events are inside.

The shape of the distribution completely changes once the sensitivity aspect is included by weighting according to (6) shown in the bottom of Fig. 10. Within the first 500-ps coincidence time window all reasonable BGO geometries have the same number of detected coincidences as the 213-ps single Gaussian LSO model.

The implementation of non Gaussian time-of-flight kernels in reconstruction was demonstrated in [32] and reconstruction results comparing BGO timing kernels [17] with a 213-ps FWHM LSO model point toward similar contrast and, due to the higher sensitivity, about 25% better SNR for the BGO model [33].

In this sense, due to the detection of Cherenkov photons, BGO can compete with L(Y)SO:Ce due to its high density and photofraction and decent timing performance while being relatively cheap, provided the timing performance achieved in the lab can be kept after system integration is done.

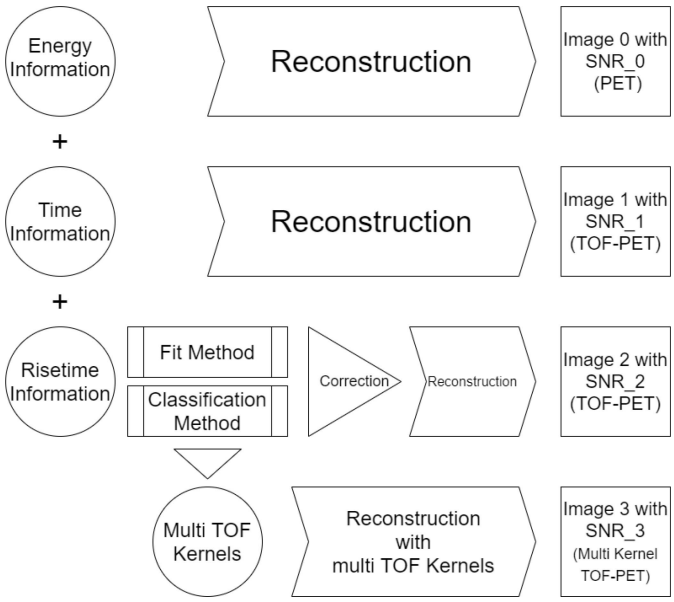

Fig. 12. Flowchart illustrating the use of information in a PET scanner leading to different image quality.

B. Multi Kernel TOF-PET

An additional advantage for the event classification comes to play when looking at individual categories more in detail, as it is done for one set of measurement for 3 × 3 × 20 mm^3 BGO coupled to HPK S14160 in this section. Three time-delay histograms for different categories are shown on the top of Fig. 11, while the CTR of all 25 categories is shown on the bottom.

The standard approach for TOF-PET is, that for a detected coincidence event the line of response (LOR) is drawn and the point of emission is determined by the time difference between the two detectors. For the results obtained with 3 × 3 × 20 mm^3 BGO coupled to HPK S14160 SiPMs this means, that each coincidence has a resolution along the LOR corresponding to a time resolution of 308 ps, i.e., 4.6 cm. However, when on both sides of the detector a high number of Cherenkov photons is detected, the time resolution of these events is better than the average. The standard approach would allocate the same position resolution to all events no matter on the real time-delay distribution. Since the RT information

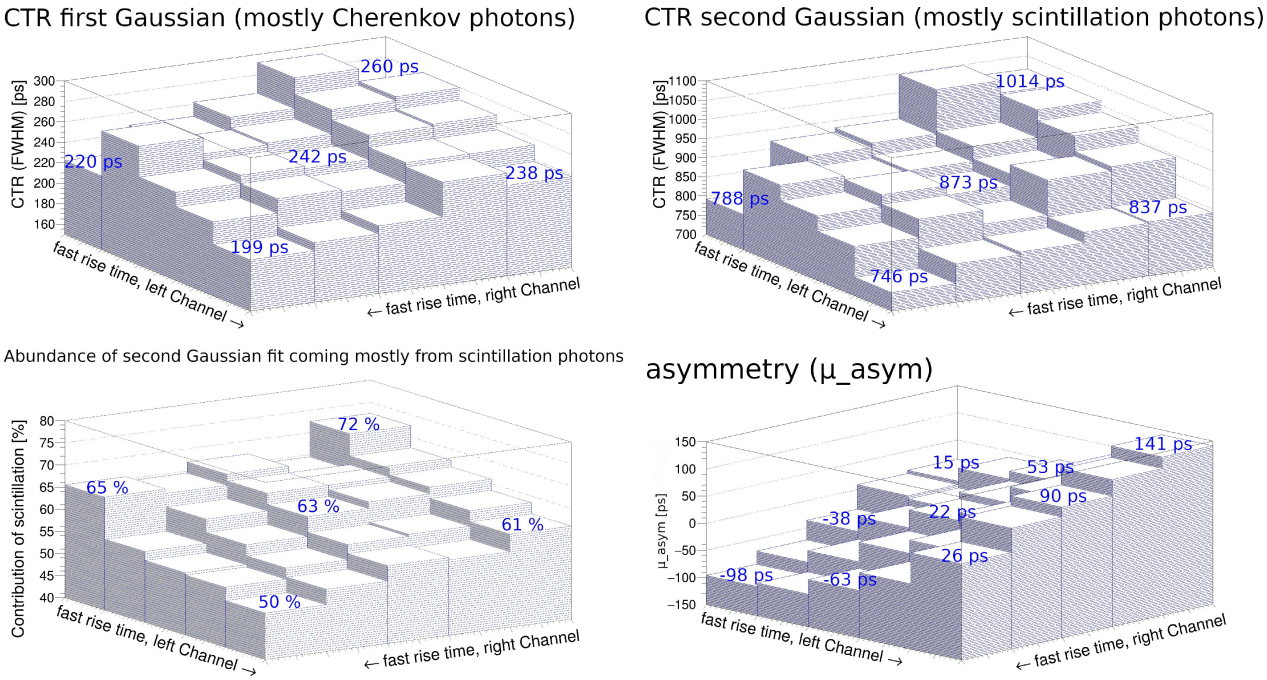

Fig. 13. Fit parameters for all 25 categories of $3 \times 3 \times 20$ mm^3 BGO coupled to HPK S14160. (top left): Time resolution of the first part of the fit function. (top right): Time resolution of the second part of the fit function. (Bottom left): Abundance of Gaussian fit coming mostly from scintillation photons [for better view $1 - r_C$ instead of r_C is plotted]. (Bottom right): Asymmetry of the time-delay distribution.

allows to classify events, a gain in SNR is expected when each category of the events is allocated to its proper kernel. This means, that events having a better time resolution can provide a better resolution along the LOR and contribute better in the reconstruction, while events with worse time resolution are used in addition to keep the high sensitivity of BGO.

The flowchart in Fig. 12 is illustrating this additional use of information leading to higher SNRs of the reconstructed image. When comparing the reconstructed images depending on the available information it is clear that $\mathrm{SNR}_2 > \mathrm{SNR}_1 > \mathrm{SNR}_0$, as the TOF information is used for image 1 and improved TOF information for image 2. However it remains an open research question to validate the gain of different TOF kernels for one LOR.

To enable reconstruction and evaluation of multi kernel TOF-PET compared to standard reconstruction the relevant fit parameters from (1), namely, the CTR of the first (top left) and second (top right) Gaussian fit function, the abundance $1 - r_C$ (bottom left) and the asymmetry term (bottom right), of all 25 categories are plotted in Fig. 13.

The classification concept demonstrated for BGO and its Cherenkov emission is not limited to this case only, but can be employed in several other cases where a distribution of timing performances is present. A prominent example is discussed in [16] having energy sharing of fast organic scintillators and inorganic scintillators giving various time resolutions depending on the energy deposition in the fast scintillator. Further improvement are expected when replacing the organic scintillator with nanostructures like CdSe [34] or $CsPbBr_3$ [35]. Another way to use the classification approach is by combining it with DOI [36], as the time resolution changes depending on the DOI position [37].

VII. Summary and Conclusion

This work investigated the potential of BGO to be used as a cost effective candidate for TOF-PET by the detection of Cherenkov emission. The non Gaussian coincidence time-delay distribution was modeled using contributions from BGO scintillation and Cherenkov emission. An event classification and correction based on the signal RT was implemented with two different correction approaches. When coupling BGO to state-of-the-art SiPMs the CTR was measured for small ($2 \times 2 \times 3$ mm^3) BGO crystals as well as with crystals matching the SiPM active area ($3 \times 3 \times 20$ mm^3) to achieve highest sensitivity in PET. We observe a degradation of time resolution in terms of FWHM and FWTM but also the individual fit contributions deteriorate when increasing the crystal cross section and/or increase the crystal length.

When accounting for the high 511-keV detection sensitivity of BGO it can be seen that BGO can compete with currently used PET systems. For example, a CTR of 215 ps FWHM for $2 \times 2 \times 15$ mm^3 BGO achieves an equivalent SNR than L(Y)SO:Ce of the same size and 127 ps CTR. Further improvements can be expected with the use of multi kernel TOF-PET reconstruction, which uses in the best statistical way the excellent CTRs achieved when detecting a high amount of Cherenkov photons. This classification approach could be a game-changing step forward in TOF-PET reconstruction with BGO, as there is no tradeoff between sensitivity and best CTR anymore.

Acknowledgment

This work has been performed in the framework of the Crystal Clear Collaboration. The authors would like to thank FBK, HPK, Ketek, and Broadcom for providing the SiPM samples used in this study and the colleagues from CERN Crystal Clear team for fruitful discussions.

REFERENCES

[1] M. Conti and B. Bendriem, "The new opportunities for high time resolution clinical TOF pet," *Clin. Transl. Imag.*, vol. 7, no. 2, pp. 139–147, 2019. [Online]. Available: https://doi.org/10.1007/s40336-019-00316-5

[2] P. Lecoq *et al.*, "Roadmap toward the 10 ps time-of-flight PET challenge," *Phys. Med. Biol.*, to be published. [Online]. Available: https://doi.org/10.1088/1361-6560/ab9500

[3] S. Gundacker, E. Auffray, K. Pauwels, and P. Lecoq, "Measurement of intrinsic rise times for various L(Y)SO and LuAG scintillators with a general study of prompt photons to achieve 10 ps in TOF-PET," *Phys. Med. Biol.*, vol. 61, no. 7, pp. 2802–2837, 2016. [Online]. Available: https://doi.org/10.1088/0031-9155/61/7/2802

[4] P. Lecoq, "Pushing the limits in time-of-flight PET imaging," *IEEE Trans. Radiat. Plasma Med. Sci.*, vol. 1, no. 6, pp. 473–485, Nov. 2017. [Online]. Available: https://doi.org/10.1109/TRPMS.2017.2756674

[5] E. J. Hoffmann, "Signal to noise improvement in PET using BGO," in *Physics and Engineering of Medical Imaging* (NATO ASI Series (Series E : Applied Sciences)), vol. 119. Dordrecht, The Netherland: Springer, 1987.

[6] J. W. Cates, S. Gundacker, E. Auffray, P. Lecoq, and C. S. Levin, "Improved single photon time resolution for analog SiPMs with front end readout that reduces influence of electronic noise," *Phys. Med. Biol.*, vol. 63, Sep. 2018, Art. no. 185022. [Online]. Available: https://doi.org/10.1088/1361-6560/aadbcd

[7] S. Gundacker, R. M. Turtos, E. Auffray, M. Paganoni, and P. Lecoq, "High-frequency SiPM readout advances measured coincidence time resolution limits in TOF-PET," *Phys. Med. Biol.*, vol. 64, no. 5, 2019, Art. no. 055012. [Online]. Available: https://doi.org/10.1088/1361-6560/aafd52

[8] P. Cherenkov, "Visible emission of clean liquids by action of γ radiation," *Dokl. Adad. Nauk SSSR*, vol. 2, no. 8, pp. 451–454, 1934.

[9] S. Gundacker, R. M. Turtos, E. Auffray, and P. Lecoq, "Precise rise and decay time measurements of inorganic scintillators by means of X-ray and 511 keV excitation," *Nucl. Inst. Methods Phys. Res. A, Accelerators Spectrometers Detectors Assoc. Equip.*, vol. 891, pp. 42–52, May 2018. [Online]. Available: https://doi.org/10.1016/j.nima.2018.02.074

[10] P. A. Williams, A. H. Rose, K. S. Lee, D. C. Conrad, G. W. Day, and P. D. Hale, "Optical, thermo-opic, electro-optic, and photoelastic properties of bismuth germanate ($Bi_4Ge_3O_{12}$)," *Appl. Opt.*, vol. 35, no. 19, pp. 3562–3569, 1996.

[11] S. Gundacker *et al.*, "Experimental time resolution limits of modern SiPMs and TOF-PET detectors exploring different scintillators and Cherenkov emission," *Phys. Med. Biol.*, vol. 65, Jan. 2020, Art. no. 025001. [Online]. Available: https://doi.org/10.1088/1361-6560/ab63b4

[12] S. E. Brunner and D. R. Schaart, "BGO as a hybrid scintillator / Cherenkov radiator for cost-effective time-of-flight PET," *Phys. Med. Biol.*, vol. 62, p. 4421, May 2017. [Online]. Available: https://doi.org/10.1088/1361-6560/aa6a49

[13] S. Kwon, E. Roncali, A. Gola, G. Paternoster, C. Piemonte, and S. R. Cherry, "Dual-ended readout of bismuth germanate to improve timing resolution in time-of-flight PET," *Phys. Med. Biol.*, vol. 64, no. 10, 2019, Art. no. 105007. [Online]. Available: https://doi.org/10.1088/1361-6560/ab18da

[14] J. W. Cates and C. S. Levin, "Electronics method to advance the coincidence time resolution with bismuth germanate," *Phys. Med. Biol.*, vol. 64, no. 17, 2019, Art. no. 175016. [Online]. Available: https://doi.org/10.1088/1361-6560/ab31e3

[15] E. Roncali, S. Kwon, S. Jan, E. Berg, and S. R. Cherry, "Cerenkov light transport in scintillation crystals explained: Realistic simulation with GATE," *Biomed. Phys. Eng. Exp.*, vol. 5 Apr. 2019, Art. no. 035033. [Online]. Available: https://doi.org/10.1088/2057-1976/ab0f93

[16] R. M. Turtos, S. Gundacker, E. Auffray, and P. Lecoq, "Towards a metamaterial approach for fast timing in PET: Experimental proof-of-concept," *Phys. Med. Biol.*, vol. 64, no. 18, 2019, Art. no. 185018. [Online]. Available: https://doi.org/10.1088/1361-6560/ab18b3

[17] N. Kratochwil, S. Gundacker, P. Lecoq, and E. Auffray, "Pushing Cherenkov PET with BGO via coincidence time resolution classification and correction," *Phys. Med. Biol.*, vol. 65, Jun. 2020, Art. no. 115004. [Online]. Available: https://doi.org/10.1088/1361-6560/ab87f9

[18] *MPPCs (SiPMs)/MPPC Arrays*. Accessed: May 26, 2020. [Online]. Available: https://www.hamamatsu.com/eu/en/product/optical-sensors/mppc/mppc_mppc-array/index.html

[19] J. A. Kolthammer, K. Su, A. Grover, M. Narayanan, D. Jordan, and R. Muzic, "Performance evaluation of the Ingenuity TF PET/CT scanner with a focus on high count-rate conditions," *Phys. Med. Biol.*, vol. 59, no. 14, pp. 3843–3859, 2014. [Online]. Available: https://doi.org/10.1088/0031-9155/59/14/3843

[20] *ROOT: Analyzing Petabytes of Data, Scientifically*. Accessed: Apr. 26, 2020. [Online]. Available: https://root.cern.ch

[21] S. Gundacker and A. Heering, "The silicon photomultiplier: Fundamentals and applications of a modern solid-state photon detector," *Phys. Med. Biol.*, vol. 65, no. 17, 2020, Art. no. 17TR01. [Online]. Available: https://doi.org/10.1088/1361-6560/ab7b2d

[22] S. Gundacker *et al.*, "State of the art timing in TOF-PET detectors with LuAG, GAGG and L(Y)SO scintillators of various sizes coupled to FBK-SiPMs," *J. Instrum.*, vol. 11, Aug. 2016, Art. no. P08008. [Online]. Available: https://doi.org/10.1088/1748-0221/11/08/P08008

[23] M. V. Nemallapudi, S. Gundacker, P. Lecoq, and E. Auffray, "Single photon time resolution of state of the art SiPMs," *J. Instrum.*, vol. 11, Oct. 2016, Art. no. P10016. [Online]. Available: https://doi.org/10.1088/1748-0221/11/10/P10016

[24] R. Dolenec, S. Korpar, P. Križan, and R. Pestotnik, "SiPM timing at low light intensities," in *Proc. IEEE Nucl. Sci. Symp. Med. Image Conf. Room-Temp. Semicond. Detector Workshop (NSS/MIC/RTSD)*, Strasbourg, France, 2016, pp. 1–5. [Online]. Available: https://doi.org/10.1109/NSSMIC.2016.8069832

[25] Z. Liu *et al.*, "In-depth study of single photon time resolution for the Philips digital silicon photomultiplier," *J. Instrum.*, vol. 11, Jun. 2016, Art. no. P06006. [Online]. Available: https://doi.org/10.1088/1748-0221/11/06/P06006

[26] S. M. Decker, M. Pizzichemi, A. Polesel, M. Paganoni, E. Auffray, and S. Gundacker, "The digital-analog SiPM approach: A story of electronic and excess noise," in *Proc. IEEE Nucl. Sci. Symp. Med. Imag. Conf. (NSS/MIC)*, Manchester, U.K., 2019, pp. 1–5. [Online]. Available: https://doi.org/10.1109/NSS/MIC42101.2019.9059792

[27] S. Gundacker, E. Auffray, P. Jarron, T. Meyer, and P. Lecoq, "On the comparison of analog and digital SiPM readout in terms of expected timing performance," *Nucl. Inst. Methods Phys. Res. A, Accelerators Spectrometers Detectors Assoc. Equip.*, vol. 787, pp. 6–11, Jul. 2015. [Online]. Available: https://doi.org/10.1016/j.nima.2014.10.020

[28] D. R. Schaart and S. Ziegler, "Achieving 10 ps coincidence time resolution in TOF-PET is an impossible dream," *Med. Phys.*, vol. 47, pp. 2721–2724, Jul. 2020. [Online]. Available: https://doi.org/10.1002/mp.14122

[29] J. L. Humm, A. Rosenfeld, and A. Del Guerra, "From PET detectors to PET scanners," *Eur. J. Nucl. Med. Mol. Imag.*, vol. 30, pp. 1574–1597, Oct. 2003. [Online]. Available: https://doi.org/10.1007/s00259-003-1266-2

[30] B. Weissler *et al.*, "A digital preclinical PET/MRI insert and initial results," *IEEE Trans. Med. Imag.*, vol. 34, no. 11, pp. 2258–2270, Nov. 2015. [Online]. Available: https://doi.org/10.1109/TMI.2015.2427993

[31] R. D. Badawi *et al.*, "First human imaging studies with the EXPLORER total-body PET scanner," *J. Nucl. Med.*, vol. 60 no. 3, pp. 299–303, 2019. [Online]. Available: https://doi.org/10.2967/jnumed.119.226498

[32] N. Efthimiou, K. Thielemans, E. Emond, C. Cawthorne, S. J. Archibald, and C. Tsoumpas, "Use of non-Gaussian time-of-flight kernels for image reconstruction of Monte–Carlo simulated data of ultrafast PET scanners," *EJNMMI Phys.*, vol. 7, p. 42, Jun. 2020. [Online]. Available: https://doi.org/10.1186/s40658-020-00309-8

[33] N. Efthimiou *et al.*, "TOF-PET image reconstruction with multiple timing kernels applied on Cherenkov radiation in BGO," Jul. 2020. [Online]. Available: https://doi.org/10.36227/techrxiv.13108238.v1.

[34] R. M. Turtos *et al.*, "On the use of CdSe scintillating nanoplatelets as time taggers for high-energy gamma detection," *npj 2D Mater. Appl.* vol. 3, p. 37. Oct. 2019. [Online]. Available: https://doi.org/10.1038/s41699-019-0120-8

[35] K. Tomanova *et al.*, "On the structure, synthesis, and characterization of ultrafast blue-emitting $CsPbBr_3$ nanoplatelets," *APL Mater.*, vol. 7, Jan. 2019, Art. no. 011104. [Online]. Available: https://doi.org/10.1063/1.5079300

[36] M. Pizzichemi *et al.*, "On light sharing TOF-PET modules with depth of interaction and 157 ps FWHM coincidence time resolution," *Phys. Med. Biol.*, vol. 64, Aug. 2019, Art. no. 155008. [Online]. Available: https://doi.org/10.1088/1361-6560/ab2cb0

[37] F. Loignon-Houle *et al.*, "DOI estimation through signal arrival time distribution: A theoretical description including proof of concept measurements," *Phys. Med. Biol.*, to be published.